GEOLOGY

Large-number detrital zircon U-Pb ages reveal global cooling caused the formation of the Chinese Loess Plateau during Late Miocene

Hanzhi Zhang[1], Huayu Lu[1]*, Jing He[1], Wanting Xie[1], Hanlin Wang[1], Hongyan Zhang[1], Daniel Breecker[2], Anna Bird[3], Thomas Stevens[4], Junsheng Nie[5], Gaojun Li[6]

The formation and evolution of the landscape of the Chinese Loess Plateau (CLP) is debated because of uncertainties regarding dust provenance. We present a quantitative estimation of dust source contributions to the CLP, based on more than 37,100 detrital zircon U-Pb ages, combined with mineral assemblages and isotope analyses. Our results reveal that the CLP was stepwise formed by ~8 million years (Ma) and is mainly composed of material from the Northeastern Qinghai-Tibetan Plateau, with stepwise shifts in relative contributions of different eolian silt sources occurring at ~2.6 Ma and 1.5 to 1.2 Ma. We infer that these changes were driven by stepwise global cooling, which induced aridification and enhanced silt production in glaciated-cold climate dust source regions, as well as dust ablation in the expanded arid regions. We propose that global cooling, rather than regional tectonic deformation, was the main driver of the formation and evolution of the CLP during late Cenozoic.

INTRODUCTION

The Chinese Loess Plateau (CLP) is a unique landscape, characterized by the most widespread, continuous, and thickest eolian deposits on Earth (Fig. 1). The Mio-Pliocene Red Clay and Quaternary loess-paleosol sequences of the CLP are archives of paleoclimatic change that are unparalleled compared with other terrestrial sediments (*1*–*3*). Understanding the formation and evolution of these eolian deposits of the CLP is essential for revealing the aridification history and the processes of dust emission and accumulation in the Asian interior, as well as the formation of this unique landscape in East Asia (*4*, *5*). However, despite a long history of study, the origin of the CLP and the provenance of the Red Clay and loess eolian silt deposits are still debated.

There are four prerequisites for the formation of the CLP: (i) a dry climate in source regions, facilitating dust emission; (ii) abundant silt production; (iii) strong and persistent dust transporting winds; and (iv) a stable and suitable land surface to accommodate the dust. The onset of dry climates in the Asian interior occurred at least since the Early Miocene (*2*) and provide the fundamental prerequisite for the CLP formation. Furthermore, the Ordos Block underlying the CLP has been tectonically stable since ~8 million years (Ma) (*6*), providing the space for eolian deposition. Despite this, the mechanism capable of producing the enormous volumes of silt deposited on the CLP and the paleo-atmospheric circulation system transporting this silt to the CLP are still unclear. The key to resolve the debate is to precisely trace the provenance of the CLP silt deposits, which enables reconstruction of the prevailing paleo-dust–transporting atmospheric circulation pattern and can improve our understanding of the mechanism and drivers of silt production and the formation of the CLP.

The silt composing the CLP is argued to be generated by high-mountain processes occurring in the surrounding orogenic belts and blocks (*7*–*11*). On the basis of modern atmospheric circulation observations (Fig. 1) (*12*) and source tracing evidence, the provenance of dust on the CLP has been suggested to be a mixture of eroded sediments from the Northeastern Qinghai-Tibetan Plateau (NQTP), the Gobi Altay Mountains (GAMs), the North China Craton (Ordos Block), and the desert and sand fields in Northern China (Fig. 1) (*8*, *10*, *11*, *13*–*15*). Some previous studies have indicated that dust source/provenance shifts occurred at ~50 Ma, ~20 Ma, ~8 Ma, 2.6 Ma, and 1.2 Ma (*4*, *16*–*18*), as well as between glacial and interglacial periods (*19*, *20*). By contrast, comprehensive analyses of Sr-Nd-Hf isotopic compositions suggest that the provenance of the CLP has remained stable since the Late Miocene, ~8 Ma (*21*). Therefore, quantitative estimates of each potential source contribution are essential to understanding the provenance and depositional processes of eolian material on the CLP.

To date, time series with quantitative estimates of the contribution of silt from different provenance areas to the CLP are sparse. Traditional bulk sample tracing methods tend to integrate the provenance signatures of multiple sources, making source apportionment difficult. Furthermore, the variation of $^{87}Sr/^{86}Sr$ ratios in eolian deposits is influenced not only by provenance shifts but also by chemical weathering and grain-size sorting (*21*). To address these limitations, we used a temporal sequence of previously unreported, large-*n* detrital zircon U-Pb age data to study the provenance and accumulation of the CLP through time. Zircon grains are resistant to weathering, and their U-Pb age distributions in sediments are effective for discriminating different provenances with multiple magmatic or high-grade metamorphic stages. The recently developed large-*n* detrital zircon U-Pb age method can provide statistically robust estimates of the relative contributions of silt from different sources (see Materials and Methods for details) (*22*) to the Chinese loess deposits. We combine this with published heavy mineral assemblage and Sr-Nd-Hf isotopic data to complement the dust provenance analyses. Although

[1]Frontiers Science Center for Critical Earth Material Cycling, School of Geography and Ocean Science, Nanjing University, Nanjing 210023, China. [2]Department of Geological Sciences, University of Texas at Austin, Austin, TX 78712-1722, USA. [3]Department of Geography, Geology and Environment, University of Hull, Hull HU6 7RX, UK. [4]Department of Earth Sciences, Uppsala University, Villavägen 16, 752 36 Uppsala, Sweden. [5]MOE Key Laboratory of Western China's Environmental Systems, Lanzhou University, Lanzhou 73000, China. [6]Frontiers Science Center for Critical Earth Material Cycling, School of Earth Sciences and Engineering, Nanjing University, Nanjing 210023, China.
*Corresponding author. Email: huayulu@nju.edu.cn

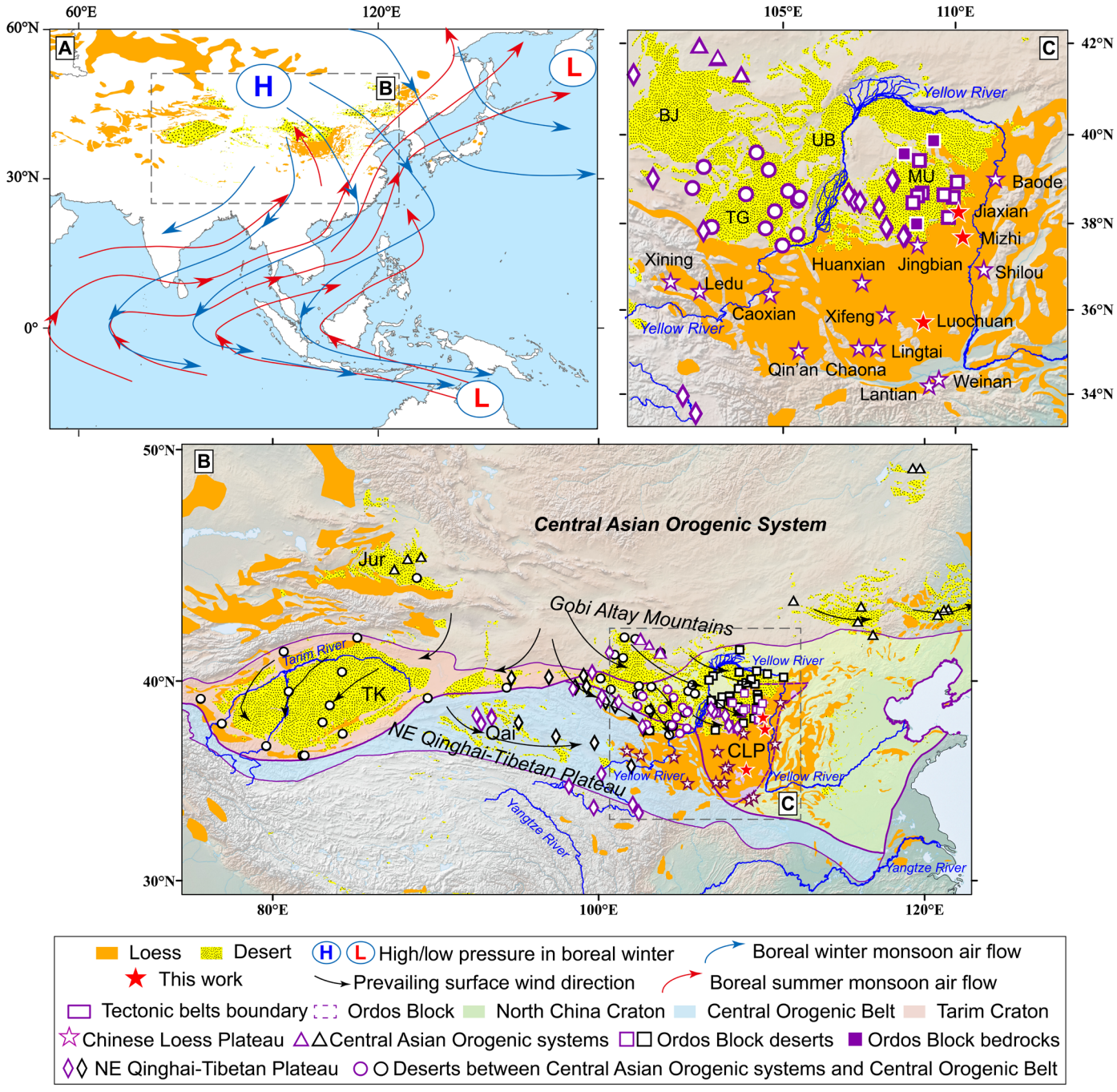

Fig. 1. Locations of the primary and secondary sources of silt particles in relation to the CLP. (**A**) Distribution of eolian deposits in Asia with the modern boreal summer and winter monsoon air flows indicated by arrows, which are cited from (*12*). (**B** and **C**) Locations referenced in this study. Red Clay and loess-paleosol sites referenced in this study are shown by purple open stars. Purple symbols refer to published sites for detrital zircon U-Pb analyses, and black symbols indicate sites with Sr-Nd-Hf isotope compositions (see Materials and Methods and table S1 for details) (*16*, *21*, *37*–*40*, *43*). MU, Mu Us sand fields; TG, Tengger Desert (Tarim Basin); BJ, Badain Jaran Desert; UB, Ulan Buh Desert; TK, Taklimakan Desert; Jur, Junggar Basin; Qai, Qaidam Basin.

there are several pioneering studies, reconstructed variations in provenance since the Late Miocene are still of relatively low temporal resolution, which introduces a risk of sample bias (*23*, *24*). Our high–time resolution, large-*n* data series covering the Late Miocene through Holocene are critical for reconstructing the formation history of the CLP.

RESULTS

Detrital zircon age spectra and the potential dust sources

Detrital zircon U-Pb age data are reported here from 99 samples from the Late Miocene to Holocene eolian silt sequences in the central and northern CLP (Fig. 2; see Materials and Methods and dataset S1 for details). The temporal resolution of the samples ranges

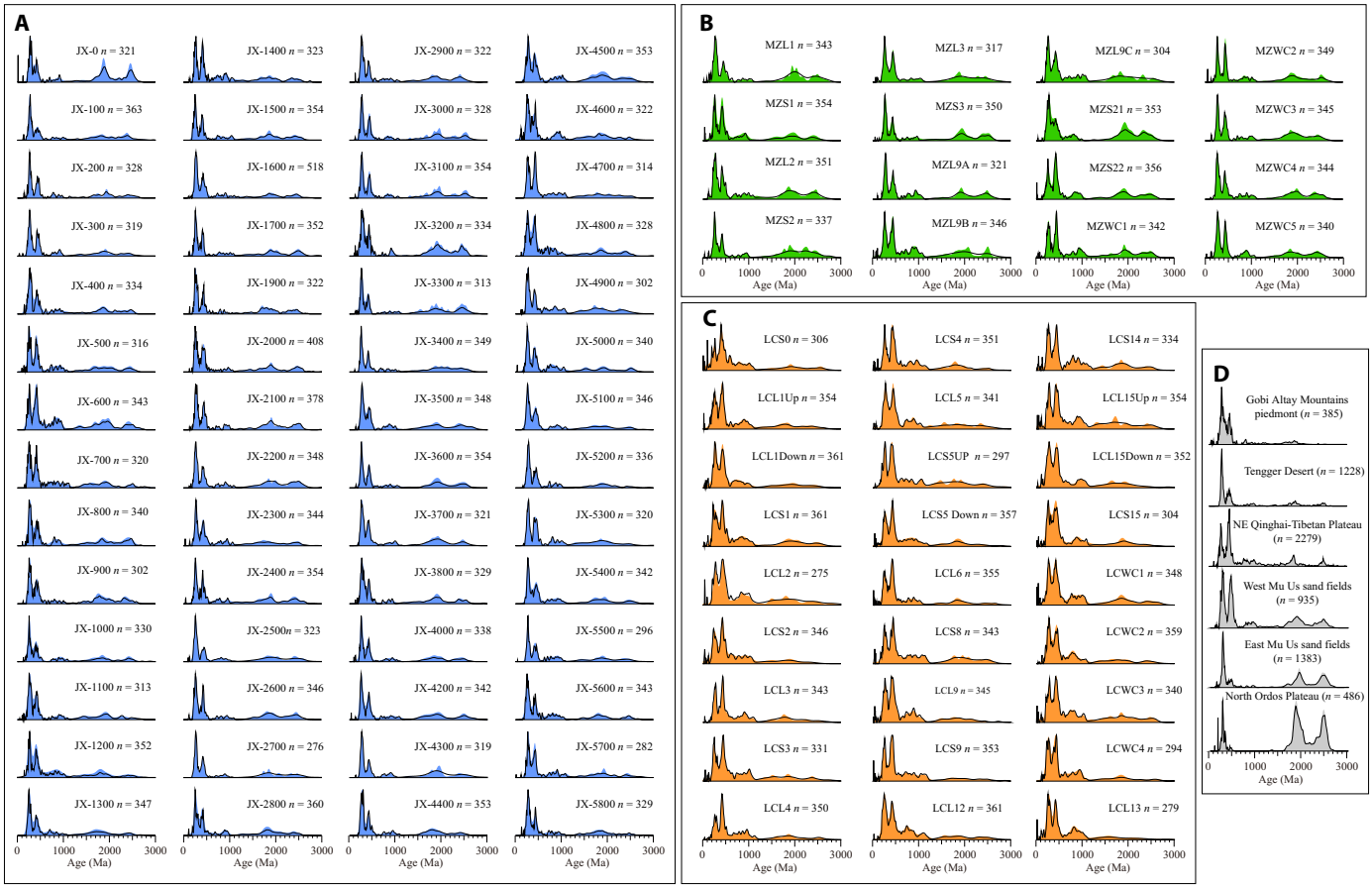

Fig. 2. Detrital zircon U-Pb ages of eolian deposits from the Jiaxian, Mizhi, and Luochuan sections and the dust source regions. The black lines are KDE and the shaded areas are PDPs (*25*). Data of Jiaxian (**A**), Mizhi (**B**) and Luochuan (**C**) is from this study. Published data of potential source regions (**D**) are collected, including the GAMs piedmont (*11*, *26*), Tengger Desert (*9*, *11*, *24*), NQTP (*10*, *20*), Mu Us sand fields (*9*, *11*), and sedimentary rocks of the north Ordos Block (*9*, *33*).

from 0.01 to 0.5 Ma over the past ~8.0 Ma. Zircon grains (309 to 552) for each sample were analyzed to characterize the relative contribution of detritus from different dust sources, and totals of more than 37,100 U-Pb ages were obtained by laser ablation inductively coupled plasma mass spectrometry (LA-ICP-MS; see Materials and Methods for details). All detrital age spectra are presented as kernel density estimates (KDE), as well as probability density plots (PDPs; Fig. 2) (*25*). The age populations of detrital zircons from the Red Clay, loess, and paleosols from the Jiaxian-Mizhi and Luochuan sections fall within four main age groups: 200 to 350 Ma, 350 to 540 Ma, 540 to 1200 Ma, and 1200 to 3000 Ma (Fig. 2 and dataset S1). The eolian deposits from the Jiaxian-Mizhi section have the most prominent peaks at 200 to 350 Ma, while the loess and paleosol samples from the Luochuan section have the most prominent peaks at 350 to 540 Ma (Fig. 2 and dataset S1).

Published detrital zircon ages from the CLP and the potential source regions (see Materials and Methods and table S1 for details) (*9*–*11*, *15*, *19*, *20*, *23*, *24*, *26*–*34*) were collected for comparison (Figs. 1 and 2D), and multidimensional scaling (MDS) (*35*) was applied to visualize the similarities (figs. S1 to S3). The MDS maps of detrital zircon age of eolian deposits in the Jiaxian-Mizhi and Luochuan-Chaona sites cluster together and with the other sites of the CLP, and they show a close similarity with the NQTP, west Mu Us sand fields, and the Tengger Desert, indicating their close genetic linkage. The eolian deposits of the CLP are relatively distant from the GAMs and east Mu Us sand fields, indicating their second-closest genetic linkage (figs. S2 and S3). Although with some possible influence of local contributions, the MDS map generally shows that the eolian silt deposits of the main body of the CLP are relatively homogeneous compared to the primary sources. Thus, the detrital zircon ages of Jiaxian-Mizhi and Luochuan-Chaona sites should be representative of the main body of the CLP (see Materials and Methods for details).

The detrital zircon U-Pb age distributions in sediments mainly result from the combined influences of regional magmatic and high-grade metamorphic events in source regions, zircon fertility of different terranes, and erosion and transportation processes (*36*). The zircon U-Pb age distributions in the source regions of the CLP are roughly consistent with the geological background of the underlying mountain belts/tectonic blocks, indicating that these source regions exert first-order control on the zircon U-Pb age distributions of the provenance sediments (see Materials and Methods and Fig. 2 for details). However, the ultrastability, high density, and relative coarse grain size (>25 μm) of the analyzed zircon particles (see Materials

and Methods for details) means that the transport sorting and recycling processes may lead to enrichment of zircon grains from the proximal sources of the NQTP and Ordos Blocks and depletion from the distal GAMs. Thus, the relative contributions from the NQTP and Ordos Blocks could potentially be overestimated solely on the basis of detrital zircon U-Pb age distributions. To avoid this bias and possible zircon fertility differences across the broad source areas, published Sr-Nd-Hf isotope data (*16*, *21*, *37*–*43*) were also collected. Three isotopic regions can be identified: the NQTP, Ordos Block, and the Central Asia Orogenic System (see Materials and Methods for details; figs. S4 and S5) (*13*, *21*). The Sr-Nd isotopic compositions of eolian samples from the CLP closely match the NQTP isotopic composition (fig. S4), while the Hf-Nd isotopic composition overlaps with all three sources (fig. S5). These observations confirm the results of the detrital zircon ages, which indicate that the eolian deposits of the CLP are essentially homogeneous and derived from the NQTP, GAMs, and Ordos Block, with the dominant contribution from the NQTP.

Quantitative estimation of the contributions from different sources

To quantitatively determine the contribution of each possible provenance area, inverse Monte Carlo modeling (*44*) was applied to data reported in this study and the published data (*9*–*11*, *20*, *23*, *24*, *26*, *33*). For each detrital age spectrum, 10,000 fitting iterations were performed to recover the contributions from potential sources, with the best-fitting 1% selected (see Fig. 3, dataset S2, and Materials and Methods for details). On the basis of the detrital zircon and isotopic tracing analyses (Fig. 2D and figs. S1, S4, and S5), the GAMs, NQTP, and Ordos Block were determined to be the three primary sources during the quantitative calculations. The western part of the Mu Us sand fields is genetically linked to the NQTP, the eastern part of the Mu Us sand fields is mainly derived from the northern Ordos Block (*9*), while the Tengger Desert shows the closest similarity to the GAMs (Fig. 2D and fig. S1) (*11*). Therefore, the detrital zircon U-Pb age data from the west Mu Us sand fields, Tengger Desert, and east Mu Us sand fields are grouped with the primary sources of the NQTP, GAMs, and Ordos Block, respectively, during the quantitative calculations (see Materials and Methods for details).

Our quantitative estimation demonstrates that the NQTP contributes 5 to 97% of the Red Clay and loess deposits (Fig. 3A), the GAMs contribute 1 to 79% (Fig. 3B), and the Ordos Block contributes 3 to 64% for the northern CLP (the Jiaxian-Mizhi sites; Fig. 3C). The NQTP contributes 62 to 98% of the eolian silt deposits (Fig. 3D), while the GAMs contribute 1 to 35% (Fig. 3E), and the Ordos Block contributes 1 to 5% for the central CLP (Luochuan-Chaona sites; Fig. 3F). The deposits in the central CLP are dominated by the NQTP contribution, while the deposits in the northern CLP received more material from the Ordos Block and GAMs sources, although the main contribution is still from the NQTP.

Temporal variations in the provenance of the CLP

The provenance of the CLP during glacial-interglacial alternations remained broadly stable, as there are no systematic differences between the provenance of loess and paleosol units, nor is there a covariation of the provenance and grain size (Fig. 3 and fig. S7). This is consistent with the Nd-Hf isotope ratios and heavy-mineral assemblage observations that suggest a consistent glacial-interglacial provenance (Fig. 3, H and I, and figs. S6 and S8) (*13*, *45*). To reveal the sedimentary evolution of dust sources to the CLP over the long term, we conducted mutation tests on the quantitative estimation results. Multiple test methods were applied, and a mutation point was accepted when more than two methods demonstrated that the result was significant at the $P < 0.05$ level (see Materials and Methods and dataset S3 for details). For the northern part of the CLP (Jiaxian-Mizhi section), the NQTP contribution had an average of 46% during ~8 to 2.6 Ma, which decreased slightly to 42% at ~2.6 Ma, and then increased to ~59% since 1.5 to 1.3 Ma (Fig. 3A). The average value of the GAMs contributions decreased from 51 to 24% and then to 10% at ~6.8 and ~1.5 Ma, respectively (Fig. 3B). The average value of the Ordos Block contribution increased from 20 to 31% at ~5.9 Ma and subsequently remained approximately the same (Fig. 3C). For the central CLP (Luochuan-Chaona sites), the NQTP contribution has an average of 78% at ~8.1 Ma, and it then increased to 91% at ~1.2 Ma (Fig. 3D). The GAMs contribution varies inversely with that of the NQTP, decreasing from 20 to 8% at ~1.2 Ma (Fig. 3E). Similarly, the Ordos Block contribution decreased from 2 to 1% at ~1.2 Ma to the central CLP (Fig. 3F). Both the northern and central sites on the CLP show a significant increase of the NQTP contribution at 1.5 to 1.2 Ma, and the northern CLP sites also show fluctuations at ~2.6 Ma.

Simultaneous shifts at ~2.6 Ma and ~1.5 to 1.2 Ma are also recorded in the detrital zircon U-Pb age data for the southern CLP (*46*), as well as in quartz $\delta^{18}O$ (*17*), $^{87}Sr/^{86}Sr$ values (Fig. 3G and fig. S6C) (*16*, *21*, *39*), and ratios of hornblende to other heavy minerals (Fig. 3J) (*45*), suggesting an increase in the physical weathering of the NQTP. The heavy-mineral assemblages (excluding hornblende) of the CLP show a relatively stable pattern since ~7 Ma (fig. S8) (*45*), indicating a relatively constant source. However, the ratios of hornblende to other heavy minerals increased in stepwise fashion at ~2.6 Ma and ~1.4 Ma, suggesting changes in the bedrock erosion rate in the NQTP (Fig. 3J) (*45*). Similarly, the compilation of Nd and Hf isotope data shows no major systematic change in the CLP since ~8 Ma (see Materials and Methods and fig. S6 for details), indicating a relatively stable provenance. Decreases in $^{87}Sr/^{86}Sr$ at ~2.6 Ma and ~1.5 to 1.2 Ma (Fig. 3G and fig. S6C) could be interpreted either as increases in the GAMs contributions relative to the NQTP (fig. S4) (*39*, *43*) or rather relate to a decrease in the weathering intensity of continental rocks (*16*, *21*). However, the former interpretation conflicts with our analyses of combined detrital zircon U-Pb ages, which show no significant increase of the GAMs contribution, which is also the case for the Nd-Hf isotopic compositions and heavy-mineral assemblages (excluding hornblende; Fig. 3 and figs. S6 and S8). On the other hand, as Sr mainly resides within easily weathered minerals, such as feldspars, intense chemical weathering leads to Sr loss and causes relatively high Rb/Sr ratios, and hence, high $^{87}Sr/^{86}Sr$ ratios (*21*). Although the presence of Sr in carbonates in the eolian deposits influences $^{87}Sr/^{86}Sr$, most carbonates in samples here were removed during pretreatment and therefore have little influence on Sr ratios (see Materials and Methods for details). We suggest that the decreases in $^{87}Sr/^{86}Sr$ in the CLP at ~2.6 Ma and ~1.5 to 1.2 Ma were caused by a reduction in the intensity of chemical weathering in the source regions, likely driven by changes in the climatic and erosional regimes of the NQTP. Furthermore, the stepwise increases in the dust accumulation rate of the CLP at ~2.6 Ma and ~1.2 Ma also suggest intensified physical weathering in the source regions (Fig. 3O and fig. S9; see Materials and Methods and dataset S4 for details).

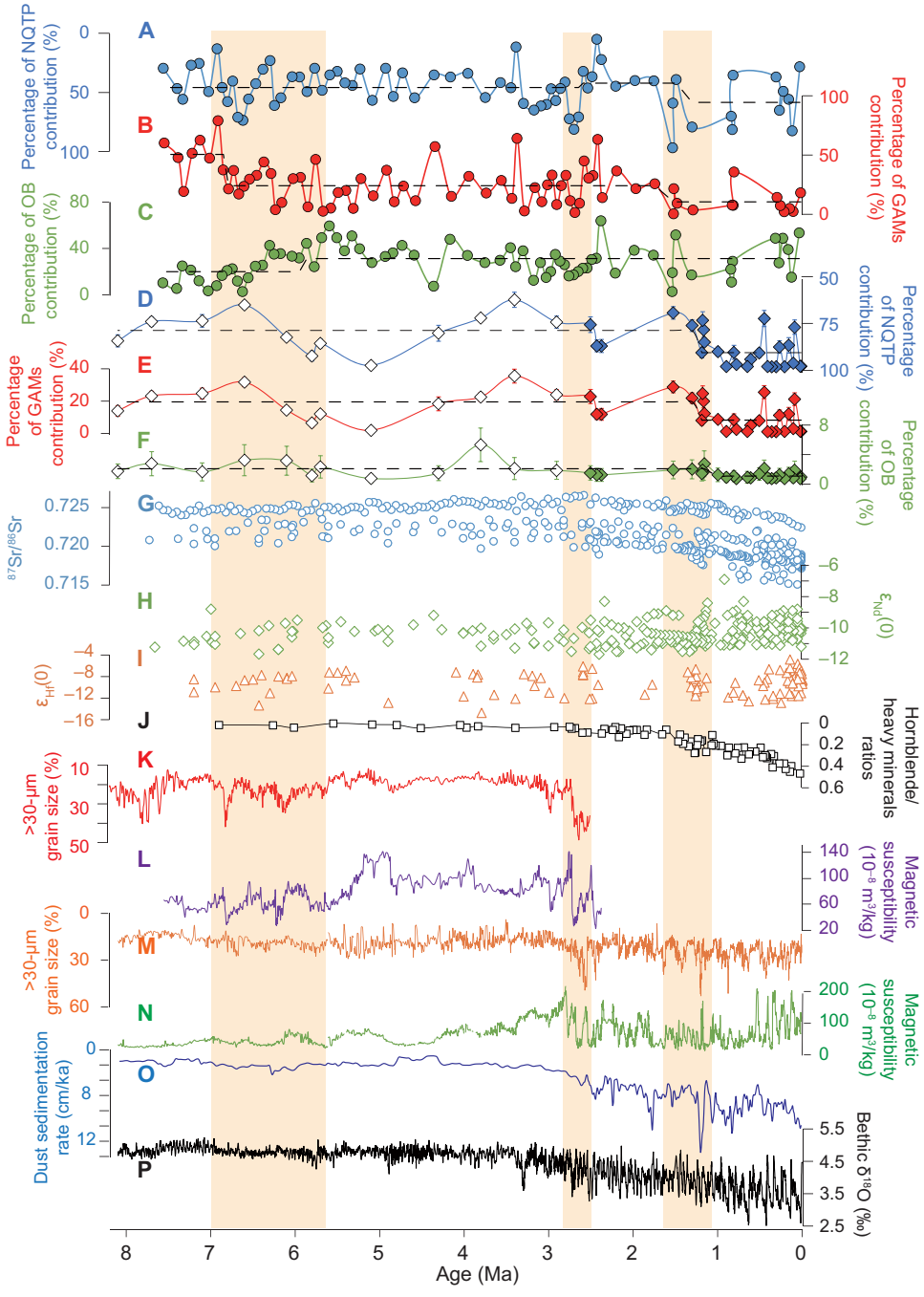

Fig. 3. Comparison of variations in provenance contributions on the CLP with regional and global paleoenvironmental records. Relative contributions of the NQTP sources (**A** and **D**), GAMs sources (**B** and **E**), and Ordos Block (OB) sources (**C** and **F**) to Jiaxian-Mizhi site (this study) (A to C), Luochuan site (this study, shown as solid diamonds), and Chaona site (*23*) (shown as open diamonds) (D to F) based on cross-correlation coefficients results derived from the PDPs (note the reversed *y* axes for the NQTP sources). (**G** to **I**) Sr (G), Nd (H), and Hf (I) isotope composition of the CLP (see Materials and Methods and table S1 for details) (*21*, *37*–*43*). (**J**) Ratios of hornblende to other heavy minerals of the eolian deposits at Lingtian on the CLP (*45*). (**K** to **N**) Percentages of the >30-μm grain-size fraction and the magnetic susceptibility record of the Jiaxian [K (*72*); L, this study] and Chaona sites (M and N) (*69*). (**O**) Average dust accumulation rate of the CLP (this study; see Materials and Methods for details). (**P**) The LR04 stacked benthic foraminiferal $\delta^{18}O$ record (10-point Locally Estimated Scatterplot Smoothing) (*51*).

DISCUSSION

The formation of the CLP has been suggested to be linked to the aridification of the Asian interior, as well as with high-mountain processes (*1*, *7*). In addition, recent work has suggested the importance of fluvial erosion and transportation of sediments (*9*, *10*, *32*). We now explore the hypothesis that global cooling was the main cause of the formation and evolution of the CLP during the late Cenozoic. We propose that the production of vast amounts of silt-sized material and the formation of the CLP were fundamentally associated with glacial grinding, cryonival fracturing, fluvial erosion, and comminution,

alongside regional aridification since the Late Miocene, dominantly in the NQTP. These processes were enhanced in a stepwise fashion by global cooling.

It has been argued that fluvial transport driven by regional precipitation was the major driver of the formation of the CLP, based on the claimed spatial heterogeneity of the silt materials of the CLP (*32*). However, although detrital zircon U-Pb age data indicate several spatial differences over the CLP—with the northern part showing a closer similarity to the Mu Us sand fields and the central part showing a greater similarity to the NQTP (Fig. 2 and fig. S3)—these differences are relatively minor compared to the differences among the primary source regions of the NQTP, GAMs, and Ordos Block (Fig. 2 and fig. S3). The two exceptions of Shilou and Dongwan (fig. S3) may reflect the impacts of locally derived sediments (*28*, *31*). Similarly, the Sr-Nd-Hf isotopic compositions of the CLP are identical over the entire CLP, compared to the relatively scattered data for the source regions (figs. S4 and S5) (*13*). We conclude that the eolian silt deposits of the CLP are relatively homogeneous compared to the primary sources, albeit with some limited spatial differences in parts, potentially driven by minor regional differences in source inputs.

Over glacial-interglacial time scales, our results show that the provenance of the CLP remains broadly similar (fig. S7). Some detrital zircon U-Pb age studies have argued for a major provenance shift and reorganization of atmospheric circulation between glacial and interglacial periods (*19*, *20*), suggesting a southward position of glacial dust transporting westerly winds over the main source regions of the CLP. However, given the data compilation here, this variation is likely an artifact of insufficient zircon U-Pb data points and/or local dust contributions. Moreover, eolian silt deposits on the CLP are mainly transported by low-level suspension transport (*7*), which means near surface winds such as the East Asian winter monsoon. Wind directions of the East Asian winter monsoon are similar between glacial and interglacial periods because of a roughly stable location of Siberia High and the Aleutian Low and Maritime Continent Low, as well as the almost constant regional topography (*3*, *5*). The East Asian winter monsoon was strengthened during the glacial period because of the increase in the contrast between high- and low-pressure systems under expanded high-latitude air masses, but overall, eolian processes and atmospheric circulation during boreal winter was roughly constant across the CLP between glacial-interglacial alternations (*3*, *5*).

On the tectonic time scale, shifts in the CLP dust provenance occurred in the Late Miocene, at ~2.6 Ma, and at 1.5 to 1.2 Ma, coinciding with the initial formation of the CLP, intensified physical erosion of the source regions, and increases in the dust accumulation rate (Fig. 3 and figs. S6 and S9) (*4*, *5*, *21*, *45*). These shifts were likely caused by changes in the processes controlling silt production, transport, and emission in the source regions, which were ultimately driven by regional tectonic uplift or climate changes. Regional uplift can increase physical erosion by creating the higher relief that promotes increased fluvial erosion and comminution and/or higher elevations for enhanced glacial grinding and cold climate physical weathering. Several lines of evidence suggest that the NQTP experienced intense uplift during 10 to 5 Ma (*47*, *48*), with the uplift of the GAMs occurring at ~5 Ma (*49*), while, in contrast, the Ordos Block remained roughly stable since the Late Miocene (*6*). These events in the primary source regions could, in principle, have increased the GAMs or NQTP contributions in the Late Miocene. However, in contrast, the observed change of the provenance signatures at 7 to 6 Ma indicates a decrease of the contribution of the GAMs and a relatively stable contribution from the NQTP but an increased contribution from the Ordos Block (Fig. 3). On the other hand, the uplift-driven topographic blocking of water vapor influx and the possible modulation of the regional atmospheric circulation could have caused the aridification of these potential dust source regions (*50*). The increased contribution from the proximal Ordos Block in the northern CLP is broadly in accord with a short-term increase of the percentage of the >30-μm grain-size fraction and decreases of the magnetic susceptibility of dust on the CLP, indicating an intensification of the East Asian winter monsoon and the weakening of the East Asian summer monsoon (EASM), respectively (Fig. 3; see Materials and Methods for details). We suggest that regional aridification caused or strengthened by tectonic processes may have influenced the contribution of silt to the northern CLP in the Late Miocene.

However, we argue that the tectonic deformation/uplift in the Late Miocene may not be the fundamental force driving the formation and evolution of the CLP. Tectonic deformations in interior Asia appear to have been asynchronous, with large uncertainties in the timing of mountain uplift events (*47*, *48*). In contrast, dust accumulation in the main part of the CLP commenced synchronously at ~8 Ma (*4*, *5*), indicating an initial formation of the CLP. On the other hand, besides the northern part of the CLP, the provenance combinations and the physical weathering intensity elsewhere in the CLP remained relatively stable during the Late Miocene through Pliocene (Fig. 3). This suggests that tectonic impacts were relatively local and were not the principal forcing mechanism for the formation and evolution of the CLP. Furthermore, there is little evidence of regional tectonic deformation/uplift since the Pliocene, and thus, the stepwise evolution of the CLP at 2.6 Ma and during 1.5 to 1.2 Ma (Fig. 3 and fig. S9) cannot be explained by tectonic forcing.

Alternatively, the initial formation of the CLP at ~8 Ma and relative synchrony of the stepwise provenance shifts, enhancement of physical erosion, weakening of chemical weathering, and the increase of the dust accumulation rate can be interpreted as a result of drying of Asian interior and intensified glaciation/periglaciation in the high mountains of the source regions, in turn a result of stepwise global cooling at 2.6 Ma and 1.5 to 1.2 Ma (Fig. 3 and figs. S6 and S9) (*4*, *5*). An arid climate is one of the prerequisites for the formation of the CLP. Regional drying not only enhances physical erosion and weakens chemical weathering of rocks but also reduces the vegetation cover, which intensifies dust emission via the enhancement of wind erosion, salt weathering, and sediment availability (Fig. 4) (*4*, *7*). Global cooling can cause reduction of the global hydrological cycle and lowering of sea level and thus cause drying in Central Asia (*4*). Multiple lines of evidence, such as the stepwise expansion of the distribution of eolian deposits, the increased dust accumulation rate (Fig. 3O), the coarsening of mean grain size of eolian deposits (Fig. 3, K and M), and other multiple proxies in the CLP, suggest that aridity in northern China was established at ~8 Ma and then intensified in a stepwise fashion ~2.6 Ma and ~1.5 to 1.2 Ma, which were synchronous with global cooling (*4*, *5*). Synchronously with global descent to the glacial climate at around 2.6 Ma, the relative fine-grained, low–sedimentation rate, and heavily weathered Red Clay was replaced by relative coarser-grained, higher–sedimentation rate, and weakly weathered loess and paleosols (*2*, *4*, *5*), indicating the establishment of the CLP. The climate of East Asia has a general northwest-to-southeast gradient (Fig. 1), with more intense aridification occurring

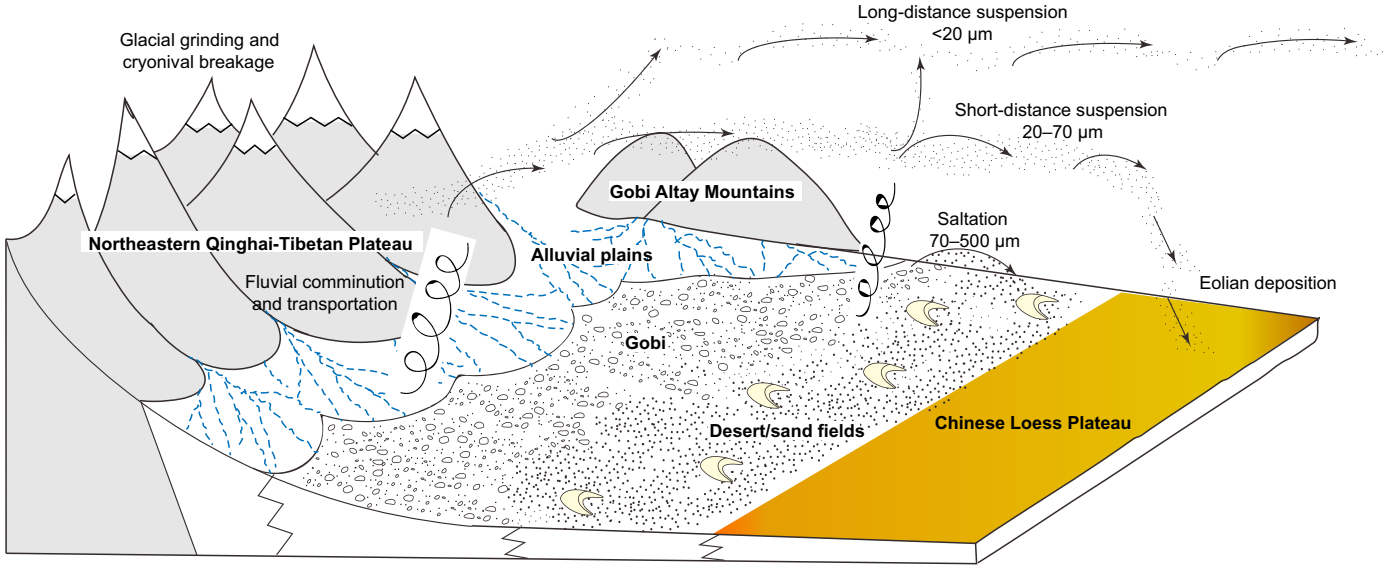

Fig. 4. Conceptual model illustrates the fundamental processes of the formation of the CLP. Rock detritus particles is mainly produced by glacial grinding, cryonival fracturing, and fluvial erosion and comminution, with the dominant contribution coming from the NQTP. These materials are transported by alluvial and fluvial systems to the piedmont and intermontane basins of the NQTP and GAMs. There, the particles are elevated by the surface winds and transported to the CLP. Sediments are sorted into different grain-size classes by local saltation transport (70 to 500 μm), short-distance suspension transport (20 to 70 μm), and long-distance suspension transport (<20 μm) (*7*). The short-distance suspension components are dominants on the CLP.

in the northwestern GAMs regions relative to the southern NQTP regions. We infer that the major sedimentary changes from Red Clay to loess and paleosol, the slight decrease of the NQTP contribution, intensified physical erosion, and weakened chemical weathering in the silt source areas of the CLP at ~2.6 Ma were mainly caused by the geographically variable aridification, forced by the global cooling (Fig. 3). The main form of the CLP was therefore established at around 2.6 Ma.

Glacial grinding, cryonival fracturing, fluvial comminution, and wind erosion in high mountains are important processes for producing silt particles (*7*). Ice volume and cold climate expanded during the glacial phases during the Pliocene-Pleistocene transition and further expanded with a larger amplitude of fluctuation at around 1.5 to 1.2 Ma (Fig. 3P) (*51*). At the same time, the contributions from the NQTP increased, the distribution of the eolian deposits expanded beyond the area of the CLP, chemical weathering decreased, and sedimentation rate/physical erosion markedly increased at 1.5 to 1.2 Ma (Fig. 3) (*4*, *5*), indicating the final formation of the landscape of the CLP. As the mountains in the NQTP are higher than 3000 m and closer to the cryosphere than the other two sources, the NQTP was more susceptible to enhanced glacial grinding and cryonival fracturing during cooling events. The enhancement of glacial/periglacial erosion at 1.5 to 1.2 Ma and the increase in regional cooling and aridity have intensified physical erosion and weakened chemical weathering. Furthermore, the relative higher relief of the NQTP likely enhanced fluvial erosion and comminution and material transport. Enormous volumes of silt can therefore be produced and efficiently transported to alluvial fans, terraces, and floodplains in the mountain piedmont and intermontane basins, where the enhanced winter monsoon and cold and dry climate in East Asia could have transported these silt sediments to the CLP (Fig. 4).

Furthermore, a persistent and intensified East Asian winter monsoon is another prerequisite for the emission and transport of eolian sediments to the CLP. The relatively stable provenance of the CLP indicates that a long-term, prevailing wind system was established by ~8 Ma. This is consistent with simulation results, which suggest the establishment of a modern-like East Asian monsoon circulation by the Early Miocene (*52*). Global cooling occurring at ~8 Ma and ~2.6 Ma caused major changes in the lower-level atmospheric circulation pattern in East Asia. These changes were fundamental to enhancing the atmospheric circulation patterns in the Pleistocene and the resultant low-level silt transporting winds responsible for most dust deposition on the CLP (*4*, *5*). The strength of the East Asian winter monsoon can be revealed by the percentage of the >30-μm grain-size fraction in eolian silts of the CLP (see Materials and Methods for details). There were marked increases in the contribution of the >30-μm grain-size fraction across the entire CLP at ~2.6 Ma and ~1.5 to 1.2 Ma (Fig. 3, K and M) (*4*), suggesting a substantial strengthening of the dust transporting agent, coeval with episodes of global cooling (Fig. 3P). These global cooling events may have enhanced the Siberian High Pressure system, causing an intensified pressure gradient between high and low latitudes and thus driving a higher frequency of dust storms, which intensified physical weathering in the arid regions and their material contribution to the CLP.

In summary, our results suggest that the eolian deposits of the CLP are mainly derived from the NQTP, GAMs, and Ordos Block, with the NQTP contributing the dominant proportion of silt particles. No glacial-interglacial alternations are detected in the provenance of the CLP deposits, while shifts in the provenance combinations occurred at ~2.6 Ma and ~1.5 to 1.2 Ma. These long-term shifts in eolian provenance and silt accumulation rate suggest that the formation and evolution of the CLP was mainly controlled by the global temperature, with regional erosion responding to this stepwise cooling since the Late Miocene. This cooling would have intensified the production and transport of enormous volumes of silt to the CLP (Figs. 1 and 4), driving its formation and evolution.

MATERIALS AND METHODS

Geological settings and age model

The eolian sequences at Jiaxian (38°5′25″ N, 110°5′25″ E) and Mizhi (37°42′1″ N, 110°12′27″ E) sites is located in the northern CLP, while the Luochuan (35°43′33″ N, 109°3′59″ E) and Chaona (35°06′ N, 107°12′ E) are located in the central CLP (Fig. 1). The chronologies of the Jiaxian-Mizhi and Chaona-Luochuan Red Clay (Late Miocene to Pliocene eolian deposits) and the loess-paleosol sequence are based on detailed magnetostratigraphy (*53*–*56*). Our time scale was built by linearly interpolating between age control points, which were based on magnetostratigraphic boundaries, with an age uncertainty of <10 thousand years (ka). These sites are selected in this study for two reasons. First, the sediments at these sites represent an "average" of the CLP, in terms of location, dust accumulation rate, grain size, and landforms. They cover both the north and central parts of the CLP, meaning that they are less affected by weathering and surface erosion, which minimizes these effects on the results of our provenance study. Second, the chronologies of these sequences are well established (*1*, *5*, *53*–*56*), providing records of the CLP evolution since ~8.0 Ma, and the age controls for all samples that we studied are robust. Fifty-six samples of Late Miocene to Pliocene Red Clay and Early Pleistocene loess and paleosols from the Jiaxian site, 16 loess-paleosol samples from the Mizhi site, and 27 loess-paleosol samples from the Luochuan site, in the central CLP, were collected for detrital zircon U-Pb dating.

Detrital zircon U-Pb age dating

Analysis of detrital zircon age distributions, which is based on the U-Pb ages of hundreds of zircon grains, is an effective means of discriminating sediment sources by the age distributions and their relative abundance. The detrital zircon U-Pb age distributions and their relative abundance are a result of the combined effects of the intensity of regional magmatic and high-grade metamorphic events, zircon fertility of different terranes, and erosional and transportation processes (*36*). Traditionally, most detrital zircon tracing studies report $n < 150$ zircon ages (*11*). However, this range limits the ability to compare the relative contributions of different sediment sources (*22*). As most of the detrital zircon U-Pb ages of potential sources in the CLP share similar age distributions, precise determination of the relative proportions of each age component is essential for the quantitative estimation of the contribution of each source. Therefore, we used a recent developed method based on a large number of zircon U-Pb ages (large-*n*), with $n > 300$ in this study, to achieve a confidence level of 95% and confirming that the grains that form populations of at least 1% or greater were represented in the age spectrum (*57*). Zircon grains (309 to 552) for each sample were analyzed, and totals of more than 37,100 U-Pb ages were obtained.

Detrital zircon grains were extracted using standard methods. First, heavy minerals in the samples were extracted by rinsing in water, and then nonmagnetic minerals were extracted using magnetic separation (*11*). The zircon grains were handpicked from the nonmagnetic heavy minerals under a microscope. More than 400 zircon grains for most samples were picked for dating, to achieve at least 300 accepted U-Pb ages for each sample. The zircon grains were mounted with epoxy resin and polished. U-Pb ages of the zircon samples were analyzed at the Laboratory of Earth Surface Processes and Environment, Nanjing University, China, using a New Wave 193-nm laser ablation system and Agilent 7700x ICP-MS. The laser beam diameter was 25 μm, with a 10-Hz repetition rate and an energy of 2 to 3 J/cm^2. The spot size enabled us to analyze detrital zircon grains larger than 25 μm (i.e., medium to coarse silt and larger). To obtain zircon ages with lower errors, the analysis pass was set to 20 s, and the pre-ablation pass to eight bursts.

Zircon 91500 (*58*) was used as the external standard for correction of isotopic fractionation, and the GJ-1 zircon (*59*) was used to monitor instrumental reproducibility and stability. NIST 610 (*60*) was used as the standard to normalize the unknown U, Th, and Pb contents. Glitter 4.4.2 (*61*) was used to process the raw data from the ICP-MS. Common Pb was corrected following the method of Andersen (*62*). All detrital zircon U-Pb age data obtained in this study are listed in dataset S1. The KDE and PDP (*25*) plots of all samples from the Jiaxian, Mizhi, and Luochuan sites are shown in Fig. 2 (A to C, respectively).

The CLP lies at the junction of the North China Craton, the Central Asian Orogenic System, and the Central Orogenic Belt (Fig. 1) (*63*). Previous investigations have shown that these three main blocks or belts are the ultimate sources for the eolian deposits of the CLP (*11*, *13*, *14*). All three blocks have experienced multiple tectonic events since the Precambrian. The terranes in the Central Orogenic Belt were relatively more active during the early Paleozoic, while the southern part of the Central Asian Orogenic System was frequently active during the late Paleozoic through early Mesozoic (*63*, *64*). The North China Craton is mainly composed of Archean crystalline basement and the Early Proterozoic Khondalite Belt (*63*, *64*). The GAMs belong to the southern part of the Central Asia Orogenic System, the NQTP belongs to the western part of the Central Orogenic Belt, and the Ordos Block comprises the southwestern part of the North China Craton (Fig. 1). These three regions are located upwind of the CLP, and therefore, we regard the GAMs, NQTP, and Ordos Block as the likely dominant direct source regions of the CLP (*11*, *13*, *14*).

To pinpoint the provenance of the eolian deposits of the CLP, we compiled published detrital zircon age data of surface samples from the piedmonts of the NQTP and GAMs, Yellow River, Qaidam Basin, Tengger Desert, Mu Us sand fields, and the Ordos Block as the source regions (Figs. 1 and 2D) (*9*–*11*, *15*, *20*, *24*, *26*, *33*). The surface samples include fluvial-alluvial plains, paleo- lacustrine deposits, top of yardang, fluvial sand, and eolian sands. The details about sample locations, lithology, and references are shown in Fig. 1 and listed in table S1. The NQTP, including the Qilian Mountains piedmont, Qaidam Basin, and the upper reaches of the Yellow River, are characterized by relatively abundant zircon grains aged 350 to 540 and 540 to 1200 Ma (Fig. 2D) (*10*, *11*, *20*, *26*). The GAMs, as well as the Tengger Desert, show dominant peaks aged 200 to 350 Ma, and relatively minor peaks at 350 to 540 Ma (Fig. 2D). The sedimentary rocks of the north Ordos Block show dominant peaks at 200 to 350 and 1200 to 3000 Ma, with a few grains with other ages (Fig. 2D) (*9*, *33*). The Mu Us sand fields are the main arid region of the Ordos Block; the western part has relatively abundant zircon grains aged 350 to 540 and 540 to 1200 Ma, while the eastern part has relatively abundant zircon grains aged 200 to 350 and 1200 to 3000 Ma (Fig. 2D) (*9*, *11*, *24*). These detrital zircon U-Pb age distribution characteristics of surface sediments are consistent with the regional magmatic and metamorphic history of the underlying craton or orogenic belts.

The zircon fertility of different terranes could cause possible bias in the detrital zircon age distributions of source regions (*36*). Magmatic rocks, which are of relatively high zircon fertility, are roughly similarly distributed in both the Central Asian Orogenic System and Central Orogenic Belt, which would contribute similar amounts of magmatic zircon grains (*63*). On the other hand, the Qaidam block

and south Qilian Mountains are involved in high-ultrahigh pressure continental collision at early Paleozoic, and amphibolite to granulite facies are relative widely distributed in these regions (*64*), which are high in zircon fertility. However, the north Qilian Mountains comprise mainly low-temperature rocks (*64*), which is extremely low in zircon fertility. The metamorphic rocks of the Central Asian Orogenic System and the main part of the Ordos Blocks are mainly greenschist to amphibolite facies, which are low in zircon fertility, although granulite, which is of high zircon fertility, is also distributed in the northwest of Ordos Blocks (*64*). Despite these differences, the sediments of these diverse potential source regions will be derived from a mixture of both high– and low–zircon fertility terranes, averaged over wide areas with wide ranging rock types. Hence, the effects of these fertility differences between parts of different source areas is hard to estimate. On the basis of the distinct characteristics of detrital zircon U-Pb age of three primary sources (Fig. 2D), we infer that the differing geological background of each larger source block is the first-order control on the zircon U-Pb age distributions of surface sediments, notwithstanding some possible influence of source rock zircon fertility differences.

MDS was used to illustrate the similarity of the sources (*35*) (fig. S1). Solid lines indicate the closest neighbors, while the dashed lines indicate the second-closest neighbors. As expected from the geological background, the MDS map of the sources shows that the NQTP, GAMs, and Ordos Block are three distinct primary sources, supporting the assertions of the secondary impact of zircon fertility outlined above. The western part of the Mu Us sand fields is genetically linked to the NQTP, while the eastern part of the Mu Us sand fields is mainly derived from the northern Ordos Block. The Tengger Desert shows the closest similarity with the GAMs (fig. S1).

Compilation of published zircon U-Pb ages and Sr-Nd-Hf isotopic data

Published zircon U-Pb ages from Baode, Jingbian, Huanxian, Lingtai, Xifeng, Weinan, Caoxian, Xining, Ledu, Dongwan, and Shilou (*15*, *19*, *20*, *24*, *26*–*31*, *34*) were compiled. The details about sample locations, lithology, and references are shown in Fig. 1 and listed in table S1. The MDS map of all the zircon age data from the CLP (including published ones and data from this study), and from the source regions, is shown in fig. S3.

Sr-Nd-Hf isotopic data of surface samples from the NQTP and the Central Asia Orogenic System, Ordos Block, Tengger Desert, Badain Jaran Desert, Tarim and Junggar basins, and Ulan Buh Desert were compiled to provide isotopic composition for possible source region endmembers (*13*, *21*, *41*, *42*). The sample locations and references are presented in Fig. 1 and table S1. The sediments from the piedmont of the NQTP, fluvial sediments from the Qaidam Basin, fluvial detritus from the NQTP, and modern fluvial sediments in the upper reach of the Yellow River are grouped as the endmember of the NQTP. The fluvial detritus of the Central Asian Orogenic System is used as the endmember of the Central Asian Orogenic System. The deserts and bedrock of the Ordos blocks are grouped as the Ordos Block endmember (Fig. 1, fig. S4, and table S1). The sediments of the NQTP are characterized by relatively low $\varepsilon_{Nd}(0)$ values and high $^{87}Sr/^{86}Sr$ ratios; the Central Asia Orogen is characterized by relatively high $\varepsilon_{Nd}(0)$ values and low $^{87}Sr/^{86}Sr$ ratios; and the Ordos Block is characterized by the lowest $\varepsilon_{Nd}(0)$ values (fig. S4) (*13*).

Few data are available for the Hf isotopic composition of the Central Asian Orogenic System. The western deserts, including the Badain Jaran Desert, Tarim and Junggar basins, and Ulan Buh Desert, are grouped as a third endmember, besides the NQTP and Ordos Blocks (Fig. 1, fig. S5, and table S1) (*13*, *21*). The Nd-Hf compositions of the source regions are overlapped, because these deserts or basins are located at the conjunction of the northern Qinghai-Tibetan Plateau, the Central Asian Orogenic System, the Ordos Block, and Tarim Craton (Fig. 1). The sediments of these regions have features of the mixing of materials from the northern Qinghai-Tibetan Plateau and Ordos Block (fig. S5).

The Sr-Nd-Hf isotopic composition data for the CLP sites of Jiaxian, Luochuan, Baode, Jingbian, Huanxian, Lingtai, Xifeng, Jingchuan, Lantian, and Qin'an were also compiled to constrain spatial and temporal changes in the provenance of the CLP (*16*, *21*, *37*–*40*, *43*) (Figs. 1 and 3 and figs. S4 to S6). The $^{87}Sr/^{86}Sr$ ratios of the eolian deposits of the CLP are argued to be determined by the detrital minerals from source regions, regional weathering, grain-size sorting, and pedogenic calcite carbonate (*65*). Thus, the selection of grain-size fraction and acid pretreatment method used to remove the primary and secondary carbonate phases in samples from the CLP would influence the interpretations of the $^{87}Sr/^{86}Sr$ ratios. For the compiled Sr-Nd-Hf isotopic composition data in this study, most of the samples were pretreated with acetic acid (*21*, *39*, *40*, *43*) or HCl (*16*), except for (*38*) and (*37*). However, the data in (*37*) refer mainly to Nd-Hf isotopes, which are not influenced by secondary carbonates. Hence, the influence of carbonate phases on the variations of the $^{87}Sr/^{86}Sr$ ratios can be excluded for these data, except for (*38*). The samples without acid pretreatment showed the lowest $^{87}Sr/^{86}Sr$ ratios (fig. S6) (*38*). Furthermore, for all the data from the source regions of the CLP, the Sr-Nd-Hf results were obtained after pretreatment with acetic acid (*21*, *41*, *42*).

Regarding the grain-size sorting effect, fine-grained clay minerals would produce high $^{87}Sr/^{86}Sr$ ratios (*65*). Some of the data were based on bulk samples (*21*, *37*, *38*, *40*), while others were based on various grain-size fractions of deposits [28 to 45 μm (*43*) and <20 μm (*16*)]. The data from (*39*) are based on both the bulk and the 28- to 45-μm fractions. Furthermore, for all the data from source regions of the CLP, the grain-size fractions were either <75 μm (*41*, *42*) or bulk samples (*21*). The $^{87}Sr/^{86}Sr$ ratios of bulk samples (*21*, *37*, *38*, *40*) were relatively higher than the 28- to 45-μm fractions (*39*, *43*) but lower than the fine fractions [fig. S6; <20 μm, (*16*)]. The detailed lithology, grain-size fractions, pretreatments, published sources, and distribution of the compiled data used in this study are presented in table S1 and Fig. 1.

To determine the temporal variations in Sr-Nd-Hf isotopic composition, multiple loess records from different references and different sites are shown in fig. S6. Figure S6 shows that the $\varepsilon_{Nd}(0)$ values on the CLP range from around −11.6 to −8.3 since ~8 Ma, with a single exception of −6.9, which is from the Lingtai L10 layer (~1 Ma) (*40*). Three samples were tested for $\varepsilon_{Nd}(0)$ in the same loess layer, and only one result has the value of −6.9 while the other two values are −9.4 and −8.9 (*40*). This high value may be due to unspecified local processes. We suggest that there was no major trend in the $\varepsilon_{Nd}(0)$ values of the CLP since ~8 Ma. The range of $\varepsilon_{Hf}(0)$ value is from around −14.7 to −6.9 during 8 to 2.6 Ma and from around −12.9 to −4.9 during the Pleistocene. The slight differences between the $\varepsilon_{Hf}(0)$ values before and after 2.6 Ma are most likely due to a sampling bias in that more studies have analyzed loess and soil units younger than 1 Ma (*21*). For most of the sites of the CLP, the $\varepsilon_{Nd}(0)$ and $\varepsilon_{Hf}(0)$ values for the same site are relative stable. We therefore suggest that both $\varepsilon_{Nd}(0)$ and $\varepsilon_{Hf}(0)$ were relatively stable within a given site

over the tectonic time scale, indicating relatively constant CLP dust sources since the Late Miocene. On the other hand, although different sites show different average values, the $^{87}Sr/^{86}Sr$ values of all the CLP sites decreased at ~2.6 and 1.5 to 1.2 Ma, indicating stepwise increases in physical weathering and decreases in chemical weathering (Fig. 3 and fig. S6).

Quantitative estimation of the provenance contributions

As discussed above, the eolian silt deposits in the CLP are mainly derived from the primary sources of the NQTP, GAMs, Ordos Block, and the secondary sources of the Tengger Desert, and the west and east Mu Us sand fields. To emphasize the variations of the contributions from the three main primary sources, based on genetic linkages and detrital zircon U-Pb age similarity (Fig. 2D and fig. S1), we grouped the detrital zircon U-Pb age dataset of the west Mu Us sand fields with that of the NQTP as the NQTP primary contribution and grouped the Tengger Desert with the GAMs as the GAMs primary contribution, and we also separated the east Mu Us sand fields to represent the primary contribution of the Ordos Block (Fig. 3, A to F).

The DZmix model, which is based on the inverse Monte Carlo method (*44*), was applied to determine the quantitative contribution of each potential source to the CLP. To match each zircon age spectrum of the eolian deposit layers from CLP, 10,000 fitting iterations were performed by varying the contributions from the potential sources, with the best-fitting 1% being selected. The Kolmogorov-Smirnov (KS) test *D* statistic and the Kuiper test *V* statistic were applied in the calculation of cumulative distribution plots, and the cross-correlation of finite mixture distributions was used to produce PDPs. The results of all the quantitative estimations of the provenance contributions and the SDs based on all three methods, as well as the cross-correlation coefficients, mean *V* values, and mean *D* values, are presented in dataset S2 and Fig. 3 and figs. S7, S10, and S11.

Quantitative estimation of the cross-correlation of PDPs was used to assess the provenances of the CLP for two reasons. First, it has been demonstrated that the cross-correlation coefficient of PDPs can contribute relatively low quantitative absolute residuals and associated SDs with fewer model trials (*44*). The SDs of the cross-correlation coefficient are broadly lower than those of the two other methods (dataset S2). Second, the cross-correlation coefficient of the PDPs is preferable when the source regions are fully investigated (*44*). As the detrital zircon ages of the source regions of the CLP have been intensively investigated, and the locations of the samples are relatively well distributed, we used the correlation coefficient results of the PDPs. The contributions of the primary sources of the NQTP, GAMs, and Ordos Block were then calculated accordingly. The cross-correlation coefficient for most of the calculation results of 99 layers of the CLP was more than 0.8, with only 13 layers having values of 0.7 to 0.8, and only 1 layer (the S0 paleosol at Luochuan) with the value of 0.667. The average of the cross-correlation coefficients at both the Jiaxian-Mizhi and Luochuan-Chaona sites was 0.86, indicating robust results. The KS test *D* statistic and the Kuiper test *V* statistic are also shown for comparison (figs. S10 and S11), as they perform better when there are uncertainties in source scaling (*44*). The results of all three methods show similar long-term variations for each provenance area.

Mutation test

To detect significant changes in the contributions from different sources, mutation tests were performed on the time series of the relative contributions from the NQTP, GAMs, and Ordos Block, obtained from the cross-correlation coefficients for the PDPs (dataset S3). The mutation test methods used included the moving *t* test method, the Cramer method, and the Yamato method (*66*). A mutation change point was lastly accepted when more than two methods showed that it was significant at $P < 0.05$. These mutations occurred at 7 to 6, ~2.6, and ~1.5 to 1.2 Ma (dataset S3).

The moving *t* method is a mutation test that assesses the differences between the mean values of two subsequences in a sequence based on the *t* value. The *t* value is calculated as follows

$$t = \frac{(\overline{x_1} - \overline{x_2})}{\sqrt{n_1^{-1} + n_2^{-1}}\sqrt{\frac{(n_1 - 1)v_1 + (n_2 - 1)v_2}{n_1 + n_2 - 2}}} \quad (1)$$

where $\overline{x_1}$ and $\overline{x_2}$ are the arithmetic mean of the two subsequences, with the length of n_1 and n_2. v_1 and v_2 are the corresponding variances. Here, n_1 and n_2 were both set as 8.

For example, there are 72 layers in the Jiaxian-Mizhi sites, with 72 results for the relative contributions of the NQTP, GAMs, and Ordos Block. Setting the results for the NQTP as a1, a2, …a72, then

$$t_1 = \frac{(\overline{x_1} - \overline{x_2})}{\sqrt{8^{-1} + 8^{-1}}\sqrt{\frac{(8 - 1)v_1 + (8 - 1)v_2}{8 + 8 - 2}}} \quad (2)$$

where $\overline{x_1}$ = (a1 + a2 + a3 + a4 + a5 + a6 + a7 + a8)/8 and $\overline{x_2}$ = (a9 + a10 + a11 + a12 + a13 + a14 + a15 + a16)/8

$$t_2 = \frac{(\overline{x_1'} - \overline{x_2'})}{\sqrt{8^{-1} + 8^{-1}}\sqrt{\frac{(8 - 1)v_1 + (8 - 1)v_2}{8 + 8 - 2}}} \quad (3)$$

where $\overline{x_1'}$ = (a2 + a3 + a4 + a5 + a6 + a7 + a8 + a9)/8 and $\overline{x_2'}$ = (a10 + a11 + a12 + a13 + a14 + a15 + a16 + a17)/8.

Then, t1, t2……t63 are obtained accordingly.

The significance level for *t* testing is set to 0.05, namely, $P = 0.05$.

$$\mathrm{tp} = \left|\mathrm{tinv}\left(\frac{p}{2}, N - 2\right)\right| \quad (4)$$

where tinv is the inverse function of the two tailed Student's *t*-distribution of N = n1 + n2, which is 16 in this study. Here, tp = 2.1448. In other words, a mutation point is detected when the *t* value is >2.1448. All *t* values obtained in this study are listed in dataset S3, and the layer with $t > 2.1448$ is shown in bold.

The Cramer method evaluates possible change points by calculating the mean value difference (d) between the subsequence and the total sequence

$$d = \left(\frac{\overline{x_{\mathrm{sub}}} - \overline{x}}{\mathrm{std}(x)}\right) \times \sqrt{\frac{n_1(n - 2)}{n - n_1\left(1 + \left(\frac{\overline{x_{\mathrm{sub}}} - \overline{x}}{\mathrm{std}(x)}\right)\right)}} \quad (5)$$

where $\overline{x}$ and $\overline{x_{\mathrm{sub}}}$ are the arithmetic mean of the total sequence and the subsequence, respectively. The subsequence is also set as eight results; std(x) is the SD of the total sequence; and n and n_1 are the corresponding sequence lengths.

The significance level is set to be the same as that for the moving *t* test. A mutation point is detected when the *t* value is >2.1448. All d values in this study are listed in dataset S3, and the layer with $d > 2.1448$ is shown in bold.

The Yamamoto method tests for a possible change point based on the mean value difference (d) between the two subsequences

$$d = \frac{|\overline{x_1} - \overline{x_2}|}{\mathrm{std}(x_1) + \mathrm{std}(x_2)} \quad (6)$$

where $\overline{x_1}$ and $\overline{x_2}$ are the arithmetic mean of the two subsequences and std(x_1) and std(x_2) are the corresponding SDs.

The significance level for t testing is set to 0.05.

$$\mathrm{Rp} = \mathrm{tp}/\mathrm{sqrt}(\mathrm{IH})$$

where tp is calculated using Eq. 4, and IH is the length of the sequence, which is set to 8. In this case, Rp is 0.7583. Similarly, a mutation point is detected when the d value is >0.7583. All d values obtained in this study are listed in dataset S3, and the layer with $d > 0.7583$ is shown in bold.

Magnetic susceptibility

The low-frequency magnetic susceptibility of loess-paleosol sequences is well accepted as an EASM proxy (*67*), as magnetic susceptibility is mainly determined by the pedogenic production of fine-grained ferromagnetic minerals. Magnetic susceptibility is therefore positively correlated to pedogenic intensity and, further, to EASM intensity. Because the Red Clay shows a similar ferromagnetic mineral assemblage to the loess-paleosol sequence, the magnetic susceptibility in the Red Clay is also regarded as an indicator of EASM strength (*3*), although there are disagreements (*68*). The low-frequency (460 Hz) magnetic susceptibility of 582 samples from the Jiaxian section was measured using a Bartington magnetic susceptibility meter. Approximately 10 g of each sample was dried at a temperature below 38°C and measured three times, and the average was taken to reduce errors. The magnetic susceptibility of the Jiaxian section was relatively low during ~7 to 5 Ma and relatively high during 5 to 3.2 Ma, and there were large fluctuations after 3.2 Ma (Fig. 3L). The magnetic susceptibility of the Chaona section is also shown (Fig. 3N) (*69*), and a similar pattern of large fluctuations is evident after ~3 Ma.

Grain size

Eolian deposits dominantly comprise 5- to 70-μm particles that are mainly transported in saltation and in short-term suspension (*7*). The percentage of the >30-μm fraction of the eolian deposits of the CLP is closely related to the intensity of the dust-transporting surface winds, and regional aridification and vegetation cover that influence dust emission and deposition (*70*), and is well accepted as a proxy of the East Asian winter monsoon strength (*71*). Grain-size data from the Jiaxian and Chaona sites were compiled to obtain a continuous record of East Asian Winter Monsoon strength (Fig. 3, K and M) (*69*, *72*).

Average dust accumulation rate in the CLP

The dust accumulation rate in the CLP is sensitive to erosion in the source regions and the wind strength of the East Asian winter monsoon. Strengthened physical weathering and wind erosion may produce more silt particles for transport and deposition on the CLP (*73*). The dust accumulation rates for the sites are calculated as the difference in depth divided by the age difference of the corresponding depths ($\Delta d/\Delta a$), with units of centimeter per thousand years. Detailed depth and age data for the Jiaxian, Xifeng, Lingtai, Chaona, and Luochuan sites, covering the main part of the CLP (Fig. 1), were obtained by linearly interpolating between the age control points, which are based on magnetostratigraphic boundaries (fig. S9) (*53*–*56*, *74*, *75*). All five sites in the CLP show relatively low dust accumulation rates during 8 to 2.6 Ma and increased rates at ~2.6 and ~1.5 to 1.2 Ma. To obtain average dust accumulation rates for the CLP, we calculated a stacked record of the dust accumulation data for five sites. The dust accumulation data for 2.581 to 0 Ma were grouped in 10-ka bins and those for 8 to 2.581 Ma into 30-ka bins, using a 50% overlap, to maintain the same age scale. Average dust accumulation rates for the CLP were then calculated on the binned time scale (Fig. 3O and dataset S4). The stacked data show similar fundamental features as the original datasets, despite the smoothing of the variations caused by the binning process (Fig. 3O and fig. S9).

SUPPLEMENTARY MATERIALS

Supplementary material for this article is available at https://science.org/doi/10.1126/sciadv.abq2007

REFERENCES AND NOTES

1. T. Liu, *Loess and the Environment* (Science Press, 1985).
2. Z. T. Guo, W. F. Ruddiman, Q. Z. Hao, H. B. Wu, Y. S. Qiao, R. X. Zhu, S. Z. Peng, J. J. Wei, B. Y. Yuan, T. S. Liu, Onset of Asian desertification by 22 Myr ago inferred from loess deposits in China. *Nature* **416**, 159–163 (2002).
3. Z. An, *Late Cenozoic Climate Change in Asia: Loess, Monsoon and Monsoon-arid Environment Evolution* (Springer Science & Business Media, 2014).
4. H. Lu, X. Wang, L. Li, Aeolian sediment evidence that global cooling has driven late Cenozoic stepwise aridification in central Asia. *Geol. Soc. Lond. Spec. Publ.* **342**, 29–44 (2010).
5. H. Lu, X. Wang, Y. Wang, X. Zhang, S. Yi, X. Wang, T. Stevens, R. Kurbanov, S. B. Marković, Chinese loess and the Asian monsoon: What we know and what remains unknown. *Quat. Int.* **620**, 85–97 (2022).
6. H. Zhao, C. Liu, Y. Yao, F. Wang, Y. Yin, Differential uplift in the west margin of Ordos Basin since Mesozoic from the fission track evidence. *J. Northw. Univ.* **37**, 470–474 (2007).
7. K. Pye, *Aeolian Dust and Dust Deposits* (Academic Press, 1987).
8. J. Sun, Provenance of loess material and formation of loess deposits on the Chinese Loess Plateau. *Earth Planet. Sci. Lett.* **203**, 845–859 (2002).
9. T. Stevens, A. Carter, T. P. Watson, P. Vermeesch, S. Andò, A. F. Bird, H. Lu, E. Garzanti, M. A. Cottam, I. Sevastjanova, Genetic linkage between the Yellow River, the Mu Us desert and the Chinese Loess Plateau. *Quat. Sci. Rev.* **78**, 355–368 (2013).
10. J. Nie, T. Stevens, M. Rittner, D. Stockli, E. Garzanti, M. Limonta, A. Bird, S. Andò, P. Vermeesch, J. Saylor, H. Lu, D. Breecker, X. Hu, S. Liu, A. Resentini, G. Vezzoli, W. Peng, A. Carter, S. Ji, B. Pan, Loess Plateau storage of Northeastern Tibetan Plateau-derived Yellow River sediment. *Nat. Commun.* **6**, 8511 (2015).
11. H. Zhang, H. Lu, X. Xu, X. Liu, T. Yang, T. Stevens, A. Bird, Z. Xu, T. Zhang, F. Lei, H. Feng, Quantitative estimation of the contribution of dust sources to Chinese loess using detrital zircon U-Pb age patterns. *J. Geophys. Res. Earth* **121**, 2085–2099 (2016).
12. J. Li, Q. Zeng, A new monsoon index, its interannual variability and relation with monsoon precipitation. *Clim. Environ. Res.* **10**, 351–365 (2005).
13. J. Chen, G. Li, Geochemical studies on the source region of Asian dust. *Sci. China Earth Sci.* **54**, 1279–1301 (2011).
14. Y. Sun, Y. Yan, J. Nie, G. Li, Z. Shi, X. Qiang, H. Chang, Z. An, Source-to-sink fluctuations of Asian aeolian deposits since the late Oligocene. *Earth Sci. Rev.* **200**, 102963 (2020).
15. T. Stevens, C. Palk, A. Carter, H. Lu, P. D. Clift, Assessing the provenance of loess and desert sediments in northern China using U-Pb dating and morphology of detrital zircons. *Geol. Soc. Am. Bull.* **122**, 1331–1344 (2010).
16. J. Sun, Nd and Sr isotopic variations in Chinese eolian deposits during the past 8 Ma: Implications for provenance change. *Earth Planet. Sci. Lett.* **240**, 454–466 (2005).
17. Y. Yan, L. Ma, Y. Sun, Tectonic and climatic controls on provenance changes of fine-grained dust on the Chinese Loess Plateau since the late Oligocene. *Geochim. Cosmochim. Acta* **200**, 110–122 (2017).
18. J. X. Li, L. P. Yue, A. P. Roberts, A. M. Hirt, F. Pan, L. Guo, Y. Xu, R. G. Xi, L. Guo, X. K. Qiang, C. C. Gai, Z. X. Jiang, Z. M. Sun, Q. S. Liu, Global cooling and enhanced Eocene Asian mid-latitude interior aridity. *Nat. Commun.* **9**, 3026–3028 (2018).
19. G. Xiao, K. Zong, G. Li, Z. Hu, G. Dupont-Nivet, S. Peng, K. Zhang, Spatial and glacial-interglacial variations in provenance of the Chinese Loess Plateau. *Geophys. Res. Lett.* **39**, L20715 (2012).

20. A. Pullen, P. Kapp, A. T. Mccallister, H. Chang, G. E. Gehrels, C. N. Garzione, R. V. Heermance, L. Ding, Qaidam Basin and northern Tibetan Plateau as dust sources for the Chinese Loess Plateau and paleoclimatic implications. *Geology* **39**, 1031–1034 (2011).
21. A. Bird, I. Millar, T. Rodenburg, T. Stevens, M. Rittner, P. Vermeesch, H. Lu, A constant Chinese Loess Plateau dust source since the late Miocene. *Quat. Sci. Rev.* **227**, 106042 (2020).
22. A. Pullen, M. Ibáñez-Mejía, G. E. Gehrels, J. C. Ibáñez-Mejía, M. Pecha, What happens when *n*= 1000? Creating large-*n* geochronological datasets with LA-ICP-MS for geologic investigations. *J. Anal. At. Spectrom.* **29**, 971–980 (2014).
23. J. Nie, A. Pullen, C. N. Garzione, W. Peng, Z. Wang, Pre-Quaternary decoupling between Asian aridification and high dust accumulation rates. *Sci. Adv.* **4**, eaao6977 (2018).
24. A. Licht, A. Pullen, P. Kapp, J. Abell, N. Giesler, Eolian cannibalism: Reworked loess and fluvial sediment as the main sources of the Chinese Loess Plateau. *Geol. Soc. Am. Bull.* **128**, 944–956 (2016).
25. P. Vermeesch, On the visualisation of detrital age distributions. *Chem. Geol.* **312-313**, 190–194 (2012).
26. X. Che, G. Li, Binary sources of loess on the Chinese Loess Plateau revealed by U-Pb ages of zircon. *Quat. Res.* **80**, 545–551 (2013).
27. H. Gong, J. Nie, Z. Wang, W. Peng, R. Zhang, Y. Zhang, A comparison of zircon U-Pb age results of the Red Clay sequence on the central Chinese Loess Plateau. *Sci. Rep.* **6**, 29642 (2016).
28. Y. Shang, C. J. Beets, H. Tang, M. A. Prins, Y. Lahaye, R. van Elsas, L. Sukselainen, A. Kaakinen, Variations in the provenance of the late Neogene Red Clay deposits in northern China. *Earth Planet. Sci. Lett.* **439**, 88–100 (2016).
29. K. Fenn, T. Stevens, A. Bird, M. Limonta, M. Rittner, P. Vermeesch, S. Andò, E. Garzanti, H. Lu, H. Zhang, Z. Lin, Insights into the provenance of the Chinese Loess Plateau from joint zircon U-Pb and garnet geochemical analysis of last glacial loess. *Quat. Res.* **89**, 645–659 (2018).
30. H. Gong, W. Xie, R. Zhang, Y. Zhang, U-Pb ages of detrital zircon and provenances of Red Clay in the Chinese Loess Plateau. *J. Asian Earth Sci.* **138**, 495–501 (2017).
31. F. Pan, J. Li, Y. Xu, M. T. D. Wingate, L. Yue, Y. Li, L. Guo, L. Guo, R. Xi, Uplift of the Lüliang Mountains at ca. 5.7 Ma: Insights from provenance of the Neogene eolian red clay of the eastern Chinese Loess Plateau. *Palaeogeogr. Palaeoclimatol. Palaeoecol.* **502**, 63–73 (2018).
32. H. Zhang, J. Nie, X. Liu, A. Pullen, G. Li, W. Peng, H. Zhang, Spatially variable provenance of the Chinese Loess Plateau. *Geology* **49**, 1155–1159 (2021).
33. Y. Chen, X. Feng, L. Chen, R. Jin, P. Miao, X. Sima, A. Miao, C. Tang, G. Wang, Z. Liu, An analysis of U-Pb dating of detrital zircons and modes of occurrence of uranium minerals in the Zhiluo Formation of northeastern Ordos Basin and their indication to uranium sources. *Geol. China* **44**, 1190–1206 (2017).
34. A. Bird, T. Stevens, M. Rittner, P. Vermeesch, A. Carter, S. Andò, E. Garzanti, H. Lu, J. Nie, L. Zeng, H. Zhang, Z. Xu, Quaternary dust source variation across the Chinese Loess Plateau. *Palaeogeogr. Palaeoclimatol. Palaeoecol.* **435**, 254–264 (2015).
35. P. Vermeesch, Multi-sample comparison of detrital age distributions. *Chem. Geol.* **341**, 140–146 (2013).
36. D. Moecher, S. Samson, Differential zircon fertility of source terranes and natural bias in the detrital zircon record: Implications for sedimentary provenance analysis. *Earth Planet. Sci. Lett.* **247**, 252–266 (2006).
37. C. Chauvel, M. Garçon, S. Bureau, A. Besnault, B. Jahn, Z. Ding, Constraints from loess on the Hf–Nd isotopic composition of the upper continental crust. *Earth Planet. Sci. Lett.* **388**, 48–58 (2014).
38. S. Gallet, B. Jahn, M. Torii, Geochemical characterization of the Luochuan loess-paleosol sequence, China, and paleoclimatic implications. *Chem. Geol.* **133**, 67–88 (1996).
39. Z. Chen, G. Li, Evolving sources of eolian detritus on the Chinese Loess Plateau since early Miocene: Tectonic and climatic controls. *Earth Planet. Sci. Lett.* **371-372**, 220–225 (2013).
40. Y. Wang, J. Yang, J. Chen, K. Zhang, W. Rao, The Sr and Nd isotopic variations of the Chinese Loess Plateau during the past 7 Ma: Implications for the East Asian winter monsoon and source areas of loess. *Palaeogeogr. Palaeoclimatol. Palaeoecol.* **249**, 351–361 (2007).
41. G. Li, T. Pettke, J. Chen, Increasing Nd isotopic ratio of Asian dust indicates progressive uplift of the north Tibetan Plateau since the middle Miocene. *Geology* **39**, 199–202 (2011).
42. G. Li, J. Chen, J. Ji, J. Yang, T. M. Conway, Natural and anthropogenic sources of East Asian dust. *Geology* **37**, 727–730 (2009).
43. W. Zhang, J. Chen, G. Li, Shifting material source of Chinese loess since ~2.7 Ma reflected by Sr isotopic composition. *Sci. Rep.* **5**, 10235 (2015).
44. K. E. Sundell, J. E. Saylor, Unmixing detrital geochronology age distributions. *Geochem. Geophys. Geosyst.* **18**, 2872–2886 (2017).
45. T. He, L. Liu, Y. Chen, X. Sheng, J. Ji, A seven-million-year hornblende mineral record from the central Chinese Loess Plateau. *Sci. Rep.* **7**, 2382 (2017).
46. H. Zhang, H. Lu, T. Stevens, H. Feng, Y. Fu, J. Geng, H. Wang, Expansion of dust provenance and aridification of Asia since ~7.2 Ma revealed by detrital zircon U-Pb dating. *Geophys. Res. Lett.* **45**, 13437–13448 (2018).
47. A. R. Duvall, M. K. Clark, E. Kirby, K. A. Farley, W. H. Craddock, C. Li, D. Yuan, Low-temperature thermochronometry along the Kunlun and Haiyuan Faults, NE Tibetan Plateau: Evidence for kinematic change during late-stage orogenesis. *Tectonics* **32**, 1190–1211 (2013).
48. D. Yuan, W. Ge, Z. Chen, C. Li, Z. Wang, H. Zhang, P. Zhang, D. Zheng, W. Zheng, W. H. Craddock, K. E. Dayem, A. R. Duvall, B. G. Hough, R. O. Lease, J. Champagnac, D. W. Burbank, M. K. Clark, K. A. Farley, C. N. Garzione, E. Kirby, P. Molnar, G. H. Roe, The growth of northeastern Tibet and its relevance to large-scale continental geodynamics: A review of recent studies. *Tectonics* **32**, 1358–1370 (2013).
49. M. Jolivet, J. Ritz, R. Vassallo, C. Larroque, R. Braucher, M. Todbileg, A. Chauvet, C. Sue, N. Arnaud, R. De Vicente, A. Arzhanikova, S. Arzhanikov, Mongolian summits: An uplifted, flat, old but still preserved erosion surface. *Geology* **35**, 871–874 (2007).
50. J. Sun, Z. Ding, W. Xiao, B. F. Windley, Coupling between uplift of the Central Asian Orogenic Belt-NE Tibetan Plateau and accumulation of aeolian Red Clay in the inner Asia began at ~7 Ma. *Earth Sci. Rev.* **226**, 103919 (2022).
51. L. E. Lisiecki, M. E. Raymo, A Pliocene-Pleistocene stack of 57 globally distributed benthic $\delta^{18}O$ records. *Paleoceanography* **20**, PA1003 (2005).
52. R. Zhang, Z. Zhang, D. Jiang, Global cooling contributed to the establishment of a modern-like East Asian monsoon climate by the early Miocene. *Geophys. Res. Lett.* **45**, 11941–11948 (2018).
53. F. Heller, T. Liu, Magnetostratigraphical dating of loess deposits in China. *Nature* **300**, 431–433 (1982).
54. G. Kukla, Loess stratigraphy in central China. *Quat. Sci. Rev.* **6**, 191–219 (1987).
55. X. K. Qiang, Z. X. Li, C. M. Powell, H. B. Zheng, Magnetostratigraphic record of the Late Miocene onset of the East Asian monsoon, and Pliocene uplift of northern Tibet. *Earth Planet. Sci. Lett.* **187**, 83–93 (2001).
56. Y. Song, X. Fang, J. Li, Z. An, D. Yang, L. Lv, Age of Red Clay at Chaona section near eastern Liupan Mountain and its tectonic significance. *Quat. Sci.* **20**, 457–463 (2000).
57. T. Andersen, Detrital zircons as tracers of sedimentary provenance: Limiting conditions from statistics and numerical simulation. *Chem. Geol.* **216**, 249–270 (2005).
58. M. Wiedenbeck, P. Allé, F. Corfu, W. L. Griffin, M. Meier, F. Oberli, A. V. Quadt, J. C. Roddick, W. Spiegel, Three natural zircon standards for U-TH-Pb, Lu-Hf, trace element and REE analyses. *Geostand. Geoanal. Res.* **19**, 1–23 (1995).
59. S. E. Jackson, N. J. Pearson, W. L. Griffin, E. A. Belousova, The application of laser ablation-inductively coupled plasma-mass spectrometry to in situ U-Pb zircon geochronology. *Chem. Geol.* **211**, 47–69 (2004).
60. N. J. G. Pearce, W. T. Perkins, J. A. Westgate, M. P. Gorton, S. E. Jackson, C. R. Neal, S. P. Chenery, A compilation of new and published major and trace element data for NIST SRM 610 and NIST SRM 612 glass reference materials. *Geostand. Geoanal. Res.* **21**, 115–144 (1997).
61. E. Van Achterbergh, C. G. Ryan, S. E. Jackson, W. L. Griffin, Data reduction software for LA-ICP-MS, in *Laser-Ablation-ICPMS in the Earth Sciences: Principles and Applications* (short course series, Mineralogical Association of Canada, 2001), vol. 29, pp. 239–243.
62. T. Andersen, Correction of common lead in U-Pb analyses that do not report ^{204}Pb. *Chem. Geol.* **192**, 59–79 (2002).
63. G. Pan, Q. Xiao, S. Lu, J. Deng, Y. Feng, K. Zhang, Z. Zhang, F. Wang, G. Xing, G. Hao, Y. Feng, Subdivision of tectonic units in China. *Geol. China* **36**, 1–28 (2009).
64. K. Bohm, T. Stevens, A. Kaakinen, Y. Lahaye, H. O'Brien, Z. Zhang, The provenance of late Cenozoic East Asian Red Clay: Tectonic-metamorphic history of potential source regions and a novel combined zircon-rutile approach. *Earth Sci. Rev.* **225**, 103909 (2022).
65. J. Chen, G. Li, J. Yang, W. Rao, H. Lu, W. Balsam, Y. Sun, J. Ji, Nd and Sr isotopic characteristics of Chinese deserts: Implications for the provenances of Asian dust. *Geochim. Cosmochim. Acta* **71**, 3904–3914 (2007).
66. R. Yamamoto, T. Iwashima, N. Sanga, Climatic change: A hypothesis in climate diagnosis. *J. Meteorol. Soc. Jpn.* **63**, 1157–1160 (1985).
67. Z. An, T. Liu, Y. Lu, S. C. Porter, G. Kukla, X. Wu, Y. Huang, The long-term paleomonsoon variation recorded by the loess-paleosol sequence in Central China. *Quat. Int.* **7**, 91–95 (1990).
68. S. Yang, Z. Ding, S. Feng, W. Jiang, X. Huang, L. Guo, A strengthened East Asian Summer Monsoon during Pliocene warmth: Evidence from 'Red Clay' sediments at Pianguan, northern China. *J. Asian Earth Sci.* **155**, 124–133 (2018).
69. L. Lü, X. Fang, J. A. Mason, J. Li, Z. An, The evolution of coupling of Asian winter monsoon and high latitude climate of Northern Hemisphere. *Sci. China Ser. D Earth Sci.* **44**, 185–191 (2001).
70. G. Újvári, J. F. Kok, G. Varga, J. Kovács, The physics of wind-blown loess: Implications for grain size proxy interpretations in Quaternary paleoclimate studies. *Earth Sci. Rev.* **154**, 247–278 (2016).
71. H. Lu, Z. An, Paleoclimatic significance of grain size of loess-palaeosol deposit in Chinese Loess Plateau. *Sci. China Ser. Earth Sci.* **41**, 626–631 (1998).
72. L. Wen, H. Lu, X. Qiang, Changes in grain-size and sedimentation rate of the Neogene Red Clay deposits along the Chinese Loess Plateau and implications for the palaeowind system. *Sci. China Ser. D* **48**, 1452–1462 (2005).

73. T. Stevens, H. Lu, Optically stimulated luminescence dating as a tool for calculating sedimentation rates in Chinese loess: Comparisons with grain-size records. *Sedimentology* **56**, 911–934 (2009).
74. Z. L. Ding, S. F. Xiong, J. M. Sun, S. L. Yang, Z. Y. Gu, T. S. Liu, Pedostratigraphy and paleomagnetism of a ~7.0 Ma eolian loess-red clay sequence at Lingtai, Loess Plateau, north-central China and the implications for paleomonsoon evolution. *Palaeogeogr. Palaeoclimatol. Palaeoecol.* **152**, 49–66 (1999).
75. D. Sun, D. Liu, M. Chen, Z. An, S. John, Magnetostratigraphy and palaeoclimate of Red Clay sequences from Chinese Loess Plateau. *Sci. China Ser. D Earth Sci.* **40**, 337–343 (1997).
76. H. Lu, F. Zhang, X. Liu, R. A. Duce, Periodicities of palaeoclimatic variations recorded by loess-paleosol sequences in China. *Quat. Sci. Rev.* **23**, 1891–1900 (2004).

Acknowledgments: We thank S. Ji, L. Serach, T. Gallagher, X. Chang, H. Lyu, L. Zhao, Y. Zhou, and S. Yi for help with field work; Y. Zhao for help with the mutation test analysis; and J. Bloemendal for polishing the English. **Funding:** This work was supported by the National Natural Science Foundation of China (41888101, 42021001, 41920104005, 41901004, and 41991321); Research Funds for the Frontiers Science Center for Critical Earth Material Cycling, Nanjing University, Fundamental Research Funds for the Central Universities (020914380102); and the National Science Foundation (PIRE 1545859). **Author contributions:** H.L. designed and organized this study. Hanzhi Zhang, H.W., Hongyan Zhang, D.B., and H.L. performed the field work. Hanzhi Zhang, J.H., and W.X. carried out the laboratory analysis. Hanzhi Zhang and H.L. wrote the manuscript. All the authors discussed and contributed to the manuscript. **Competing interests:** The authors declare that they have no competing interests. **Data and materials availability:** All data needed to evaluate the conclusions in the paper are present in the paper and/or the Supplementary Materials.

Submitted 24 March 2022
Accepted 24 August 2022
Published 12 October 2022
10.1126/sciadv.abq2007